Microsc. Microanal. 12, 191–205, 2006
DOI: 10.1017/S1431927606060326

Microscopy AND Microanalysis

Progress in Aberration-Corrected High-Resolution Transmission Electron Microscopy Using Hardware Aberration Correction

Markus Lentzen*

Institute of Solid State Research, Ernst Ruska Centre for Microscopy and Spectroscopy with Electrons, Research Centre Jülich, 52425 Jülich, Germany

Abstract: The design and construction of a double-hexapole aberration corrector has made it possible to build the prototype of a spherical-aberration corrected transmission electron microscope dedicated to high-resolution imaging on the atomic scale. The corrected instrument, a Philips CM200 FEG ST, has an information limit of better than 0.13 nm, and the spherical aberration can be varied within wide limits, even to negative values. The aberration measurement and the corrector control provide instrument alignments stable enough for materials science investigations. Analysis of the contrast transfer with the possibility of tunable spherical aberration has revealed new imaging modes: high-resolution amplitude contrast, extension of the point resolution to the information limit, and enhanced image intensity modulation for negative phase contrast. In particular, through the combination of small negative spherical aberration and small overfocus, the latter mode provides the high-resolution imaging of weakly scattering atom columns, such as oxygen, in the vicinity of strongly scattering atom columns. This article reviews further lens aberration theory, the principle of aberration correction through multipole lenses, aspects for practical work, and materials science applications.

Key words: high-resolution transmission electron microscopy, aberration measurement, aberration correction, contrast theory, phase contrast

Introduction

In high-resolution transmission electron microscopy, lens aberrations play a key role in the imaging and the interpretation of object structures on an atomic scale. Aberrations are beneficial and detrimental to high-resolution imaging at the same time: On the one hand, they introduce unwanted blurring in any imaging plane, hence obscuring the finest object details. On the other hand, they are urgently needed to produce the desired phase contrast of the very thin objects required for high-resolution structure investigations.

Foremost among all aberrations in the electron microscope is the strong and fixed spherical aberration of the objective lens. In his famous paper on the theoretical resolution limit of the electron microscope of 1949, Scherzer calculated the so-called point resolution for the beneficial phase contrast from thin objects, if proper defocus of the objective lens, the Scherzer defocus, is applied (Scherzer, 1949). The point resolution is then only dependent on the electron wavelength and the constant of spherical aberration. Therefore, improvement of the point resolution can only be achieved through a shorter wavelength at higher acceleration voltages or by reducing the spherical aberration. The latter is only possible within certain limits, because the spherical aberration coefficient of a round lens is always positive and on the order of its focal length (Scherzer, 1936). Despite many instrumental improvements over the decades, advancing the information limit to the sub-Ångström range, around 0.8 Å for a 300-kV instrument (O'Keefe et al., 2001; Kisielowski et al., 2001), the point resolution of standard electron microscopes equipped with round lenses stagnated at values of about 1 Å for high-voltage microscopy and at about 1.6 Å for medium-voltage microscopy.

Direct and indirect solutions to the spherical aberration problem have been proposed, but they remained impractical for a long time. Gabor devised the elegant concept of electron holography (Gabor, 1949) with the key idea of recording an electron hologram in an electron microscope with strong positive spherical aberration, thus storing the full information in the scattered electron wave altered by the lens aberration. In a second step the hologram information, stored on a photographic plate, should then be reconstructed in a light-optical device with negative spherical aberration, thus restoring the scattered electron wave unaltered by the lens aberration and providing an undisturbed

Received February 3, 2005; accepted February 13, 2005.
*E-mail: m.lentzen@fz-juelich.de

structure image. Gabor's concept soon yielded fruit in light optics (Leith & Upatnieks, 1962, 1963, 1964), but not until 40 years later with the advent of electron sources with improved coherence in high-resolution electron microscopy (Lichte, 1986; Tonomura, 1993).

A variant of the holographic restoration of the undisturbed scattered electron wave was proposed by Schiske in 1968, with the idea of changing the lens defocus systematically and measuring the image intensity at many imaging planes (Schiske, 1968, 2002; Saxton, 1978, 1988; Van Dyck et al., 1993). Each image represents an in-line hologram, in terms of Gabor's formalism, and an unambiguous solution of the reconstruction problem can be found by using a set of filters to deduce the complex electron wave from the image series. The method and its variants became useful for high-resolution structure investigations in the 1990s, when more powerful digital computers became available (Coene et al., 1992, 1996; Saxton, 1994; Thust et al., 1996*a*).

A direct instrumental approach to the spherical-aberration problem was already proposed by Scherzer: The use of multipole lenses provides a way to produce a diverging lens system with negative spherical aberration, thus compensating the positive spherical aberration of the objective lens (Scherzer, 1947). Due to technical difficulties, however, several attempts to improve the optical performance of a high-resolution transmission electron microscope have failed.

This review reports on the recent successful attempt at multipole aberration correction of a medium-voltage transmission electron microscope, the Philips CM200 FEG ST, operated at an accelerating voltage of 200 kV (Haider et al., 1998*c*). An overview of the important lens aberrations, the principle of spherical aberration correction with a multipole aberration corrector, aberration measurement, and corrector alignment, contrast transfer and new imaging modes in the corrected microscope, hints for practical work, and materials science applications are also described.

The spherical-aberration problem exists as well in the related technique of scanning transmission electron miscoscopy (STEM), which is beyond the scope of this review due to the different electron-optical construction of that microscopes and due to the different electron-optical approach to spherical-aberration correction (Dellby et al., 2001; Batson et al., 2002).

Lens Aberrations

For an ideal lens, rays originating from an object point converge at a single image point. In the equivalent wave picture, the spherical wave originating from a point object is transformed by the ideal lens to a spherical wave converging toward the image point. Imperfect lenses are described in the first system by ray aberrations and in the second system by wave aberrations (Born & Wolf, 1980). The ray aberration of a ray leaving the object point with a diffraction vector $\boldsymbol{g}$ is given by the displacement vector $\boldsymbol{R}(\boldsymbol{g})$ from the ideal Gaussian image point to the point where the ray, after passing through the lens, intersects the image plane. The wave aberration $\chi(g)$ is the deviation of the wavefront, imposed by the lens, from the ideal reference sphere converging toward the ideal image point. The deviation of the wave front is expressed by an additional phase shift between the wave function in the object plane $\psi_{\mathrm{obj}}(\boldsymbol{g})$ and the wave function in the image plane $\psi_{\mathrm{im}}(\boldsymbol{g})$,

$$\psi_{\mathrm{im}}(\boldsymbol{g}) = \psi_{\mathrm{obj}}(\boldsymbol{g})\exp(-2\pi i\chi(\boldsymbol{g})). \tag{1}$$

The aberration function $\chi(\boldsymbol{g})$ can be written in compact form, if $\boldsymbol{g}$ is expressed as a complex number, $\boldsymbol{g} = g_x + ig_y$, and the related complex scattering angle, $\boldsymbol{\omega} = \lambda\boldsymbol{g}$, with λ being the electron wavelength, is used (see, e.g., Uhlemann & Haider, 1998). Expanding $\chi(\boldsymbol{g})$ to fifth order in $\boldsymbol{g}$ and substituting $\boldsymbol{g}$ by $\boldsymbol{\omega}$ yields

$$\begin{aligned}\chi(\boldsymbol{\omega}) = 1/\lambda\ \mathrm{Re}\{&\tfrac{1}{2}C_{10}\boldsymbol{\omega}\bar{\boldsymbol{\omega}} + \tfrac{1}{2}C_{12}\bar{\boldsymbol{\omega}}^2 + \tfrac{1}{3}C_{21}\boldsymbol{\omega}\bar{\boldsymbol{\omega}}^2\\ &+ \tfrac{1}{3}C_{23}\bar{\boldsymbol{\omega}}^3 + \tfrac{1}{4}C_{30}\boldsymbol{\omega}^2\bar{\boldsymbol{\omega}}^2 + \tfrac{1}{4}C_{32}\boldsymbol{\omega}\bar{\boldsymbol{\omega}}^3\\ &+ \tfrac{1}{4}C_{34}\bar{\boldsymbol{\omega}}^4 + \tfrac{1}{5}C_{41}\boldsymbol{\omega}^2\bar{\boldsymbol{\omega}}^3 + \tfrac{1}{5}C_{43}\boldsymbol{\omega}\bar{\boldsymbol{\omega}}^4\\ &+ \tfrac{1}{5}C_{45}\bar{\boldsymbol{\omega}}^5 + \tfrac{1}{6}C_{50}\boldsymbol{\omega}^3\bar{\boldsymbol{\omega}}^3 + \tfrac{1}{6}C_{52}\boldsymbol{\omega}^2\bar{\boldsymbol{\omega}}^4\\ &+ \tfrac{1}{6}C_{54}\boldsymbol{\omega}\bar{\boldsymbol{\omega}}^5 + \tfrac{1}{6}C_{56}\bar{\boldsymbol{\omega}}^6\},\end{aligned} \tag{2}$$

with the lens aberration coefficients defocus C_{10}, twofold astigmatism C_{12}, second-order coma C_{21}, threefold astigmatism C_{23}, third-order spherical aberration C_{30}, third-order star aberration C_{32}, fourfold astigmatism C_{34}, fourth-order coma C_{41}, three-lobe aberration C_{43}, fivefold astigmatism C_{45}, fifth-order spherical aberration C_{50}, fifth-order star aberration C_{52}, rosette aberration C_{54}, and sixfold astigmatism C_{56}. The lens aberration coefficients C_{nk} are complex numbers denoting the two Cartesian components, excepting C_{10}, C_{30}, and C_{50}, which are real numbers, and $\bar{\boldsymbol{\omega}}$ denotes the complex conjugate of $\boldsymbol{\omega}$.

Different systems can be found in the literature to denote aberration coefficients (e.g., compare Bernhard, 1980; Uhlemann & Haider, 1998; Saxton, 2000). In this review, we have used indices n and k to denote order and azimuthal symmetry of the aberration C_{nk}. Following the suggestion of Saxton (2000), factors $1/(n+1)$ were used for all contributions to the nth order.

The ray aberration is linked to the wave aberration by

$$\boldsymbol{R}(\boldsymbol{\omega}) = 2\partial\chi(\boldsymbol{\omega})/\partial\bar{\boldsymbol{\omega}} \tag{3}$$

(Lichte, 1991; Coene & Jansen, 1992).

In traditional electron microscopy, aberration correction is limited first to finding the coma-free axis of the objective lens by using an intentional illumination tilt and then eliminating twofold astigmatism by using the objective lens stigmators. The large, positive, and fixed third-order spherical aberration, which is on the order of the focal length of the objective lens, is combined with a favorable defocus setting $Z = C_{10}$ to form the Scherzer $\lambda/4$ phase plate,

$$Z_{\mathrm{Sch}} = -(\tfrac{4}{3} C_{30}\, \lambda)^{1/2}, \tag{4}$$

with the point resolution

$$d_{\mathrm{Sch}} = (\tfrac{3}{16} C_{30}\, \lambda^3)^{1/4}, \tag{5}$$

so that object information up to a spatial frequency $1/d_{\mathrm{Sch}}$ is transferred with the same sign of the aberration function, yielding dark-atom contrast for a thin specimen. The use of factors $\frac{4}{3}$ and $\frac{3}{16}$ in the above equations extends the point resolution slightly, as in the treatment of Eisenhandler and Siegel (1966), compared with the original Scherzer defocus (Scherzer, 1949). The Scherzer phase plate is the equivalent of the Zernike phase plate in light optics (Zernike, 1942*a*, 1942*b*, 1955): The weak potential of thin specimens imposes a phase change of the scattered electron wave by $\pi/2$ with respect to the transmitted wave, and the additional phase change of the objective lens by another $\pi/2$ produces a structure image with positive phase contrast.

In addition, Lichte's defocus of least confusion (Lichte, 1991)

$$Z_{\mathrm{L}} = -\tfrac{3}{4} C_{30}\, \lambda^2 g_{\max}^2 \tag{6}$$

denotes the imaging plane where the largest ray displacement $R_{\max}(\boldsymbol{g})$ inside an aperture given by the information limit $g_{\max}$ has a minimum, that is, the respective bundle of rays inside the aperture has a minimum delocalization of

$$R_{\mathrm{L}} = \tfrac{1}{4} C_{30}\, \lambda^3 g_{\max}^3. \tag{7}$$

Another important setting is the minimum phase-contrast defocus (Heinemann, 1971)

$$Z_{\min} = -(\tfrac{1}{4} C_{30}\, \lambda)^{1/2} \tag{8}$$

transferring information from a thin object up to a spatial frequency

$$g_{\min} = (C_{30}\, \lambda^3)^{-1/4} \tag{9}$$

with contrast close to zero. This defocus is important to establishing an easily detectable reference in order to set the objective lens either to Scherzer defocus or Lichte's defocus of least confusion.

As the information limit of transmission electron microscopes has improved, chiefly by the use of field-emission electron guns, the importance of correcting threefold astigmatism became apparent (Typke & Dierksen, 1995). This problem was soon solved by incorporating a respective stigmator to compensate for the fixed threefold astigmatism of the objective lens (Wang et al., 1999). At the same time, the influence of higher-order aberrations, such as third-order star aberration, C_{32}, or fourfold astigmatism, C_{34}, did not seem to be important for high-resolution materials science investigations.

Because of the improving information limit of field-emission instruments, the discrepancy between information limit on the one hand and point resolution and minimum delocalization on the other hand increased. For a modern 300-kV instrument with $C_{30} = 0.6$ mm and an information limit of 0.1 nm, the point resolution amounts to only 0.17 nm and the smallest delocalization to even 1.2 nm! For such an instrument operated at Scherzer defocus, rapid contrast reversals occur at spatial frequencies between the Scherzer limit and the information limit, impairing intuitive structure interpretation for a thin object (Lichte, 1991; Coene & Jansen, 1992). At Lichte's defocus, minimizing delocalization, a number of contrast reversals appear over the entire frequency range (Lichte, 1991). The comparably poor point resolution and the contrast reversals are due to the strong spherical aberration, which in the above case contributes 12 full cycles of the aberration function.

Figure 1A–C provides an overview of phase contrast transfer functions for Scherzer defocus and an instrument equipped with a LaB_6 source, for Scherzer defocus and improved spatial coherence with an FEG source, and Lichte's defocus of least confusion. The calculations assume an acceleration voltage of 200 kV and a large spherical aberration of 1.23 mm. Table 1 gives the corresponding defocus settings and the resulting values for the delocalization in the image plane.

Two indirect methods for aberration correction, and in particular for spherical-aberration correction, became feasible in the 1990s: high-resolution electron holography (Lichte, 1986; Tonomura, 1993) and through-focus series reconstruction (see, e.g., Coene et al., 1992, 1996; Saxton, 1994; Thust et al., 1996*a*, 1996*b*). Both methods measure the exit wave function in the image plane, $\psi_{\mathrm{im}}(\boldsymbol{g})$, which is then used to restore the exit wave in the object plane, $\psi_{\mathrm{obj}}(\boldsymbol{g})$, by applying a numerical phase-plate $\exp(-2\pi i \chi(\boldsymbol{g}))$ determined from an independent measurement of the aberration function $\chi(\boldsymbol{g})$ (Thust et al., 1996*b*; Lehmann, 2000; Saxton, 2000). The restored exit wave in the object plane is almost free of delocalization and yields atomic structure detail out to the information limit of the microscope. A very small residual delocalization, which is, in practice, smaller than the blurring due to the finite information limit, results from the small, unavoidable errors of the aberration measurement.

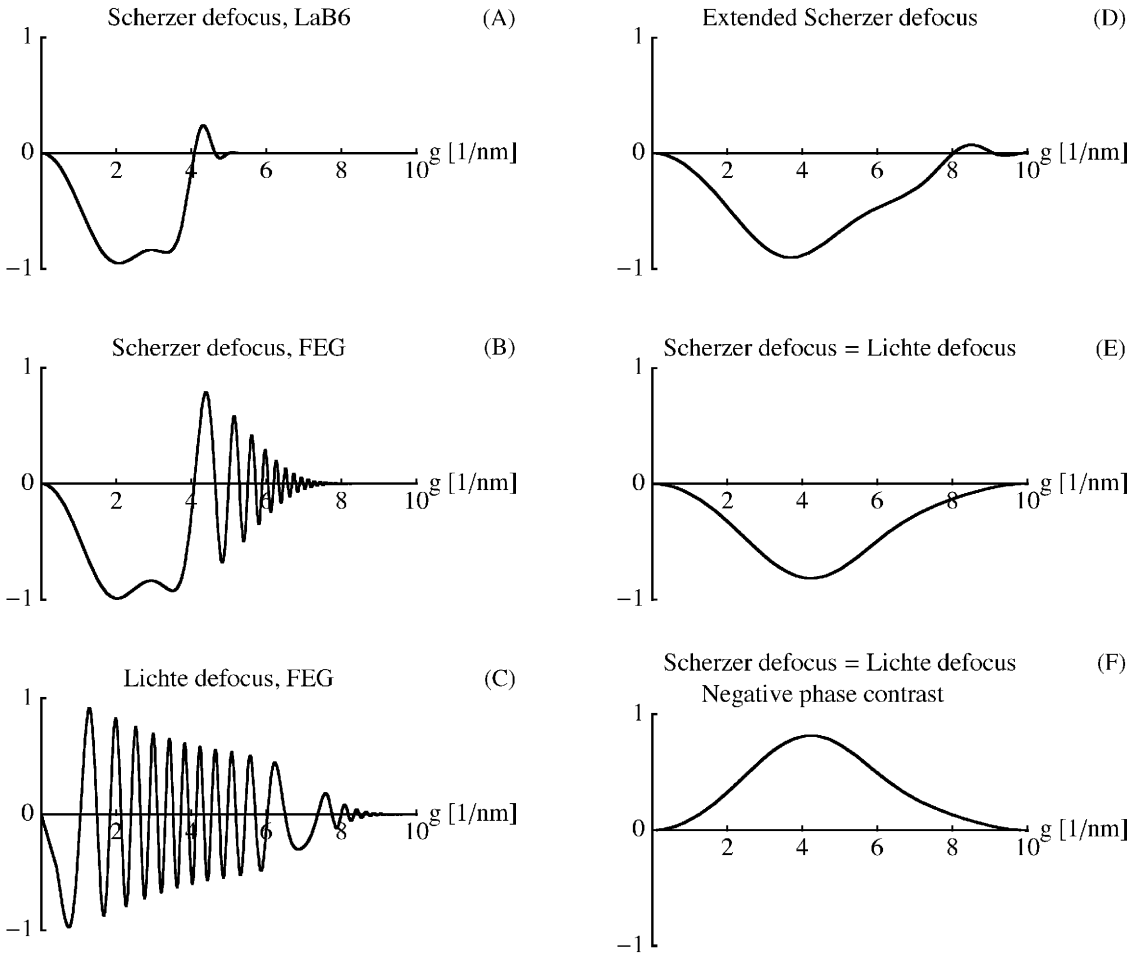

Figure 1. Typical phase contrast transfer functions for an acceleration voltage of 200 kV. **A:** Scherzer defocus, LaB_6 source, large positive spherical aberration. **B:** Scherzer defocus, FEG source, large positive spherical aberration. **C:** Lichte defocus, FEG source, large positive spherical aberration. **D:** Scherzer defocus, FEG source, small positive spherical aberration. **E:** Scherzer defocus = Lichte defocus, FEG source, small positive spherical aberration. **F:** Scherzer defocus = Lichte defocus, FEG source, small negative spherical aberration.

Table 1. Delocalization, R, for 200 kV Microscopes with LaB_6 and FEG Sources, and for Different Settings of Defocus, Z, and Spherical Aberration, C_3

	Z (nm)	C_3 (mm)	R (nm)
Scherzer defocus, LaB_6	−64	1.23	0.65
Scherzer defocus, FEG	−64	1.23	4.2
Lichte defocus, FEG	−371	1.23	2.5
Extended Scherzer defocus, FEG	−17	0.083	0.33
Scherzer defocus = Lichte defocus, FEG	−11	0.037	0.07

There was still a need for a direct solution to the delocalization problem: The indirect exit-wave reconstruction methods were not able to provide the microscope operator with a fast and direct view of the object structure at the location of interest. Direct lens correction was expected to reveal such an image, and a project on lens aberration correction of a medium-voltage transmission electron microscope started in 1992 with the aim of showing the potential of lens correction for high-resolution materials science investigations (Haider et al., 1995). The project was based on an outline for an aberration corrector by Rose (1990, 1994).

Multipole Aberration Corrector

For many years, spherical aberration correction of the imaging system of a transmission electron microscope seemed to be impossible. Scherzer had already shown that such correction of a round objective lens cannot be made, in principle, without the use of fields varying with time, space charges,

or multipoles (Scherzer, 1936). The use of space charges and fields varying with time proved to be impractical for transmission electron microscopy, and the use of multipole fields was not accessible for a long time due to the stringent requirements for electrical stability.

A project on the correction of a transmission electron microscope started in the mid-1970s (Bastian et al., 1971; Rose, 1971; Heinzerling, 1976; Koops et al., 1976; Kuck, 1979; Bernhard, 1980; Fey, 1980; Hely, 1982*a*, 1982*b*), where the demands on the correcting lens system were particularly high, because not only did imaging from a single point in the object plane have to be successfully corrected but also imaging of a wide field of such points. The project aimed not only at spherical aberration correction but also at the simultaneous correction of chromatic aberration at an accelerating voltage of 40 kV. The layout of the corrector system consisted of five magnetic octupoles; the three center elements were combined magnetic and electric octupoles. Spherical aberration correction and chromatic aberration correction were successfully demonstrated. The corrected instrument reached an information limit of 1.5 nm imposed not by residual aberrations, but by the electrical and mechanical instabilities of the uncorrected microscope.

A second project started in 1992 with the aim of correcting spherical aberration in a 200-kV transmission electron microscope (Rose, 1990; Haider et al., 1995). The correcting system consisted of two hexapoles and four additional round lenses. Its advantage over the former layout was a stability requirement for the hexapole fields of about 10 ppm, which was two orders of magnitude lower than for quadrupole fields (Haider et al., 1998*a*). The lack of chromatic aberration correction in this layout was partly compensated by the use of a microscope equipped with a field-emission gun, thus providing a smaller electron energy spread and hence a much smaller contribution to the temporal coherence envelope.

The principle of spherical aberration correction using the double-hexapole corrector (Beck, 1979; Rose, 1990; Haider et al., 1995) can be understood by considering first the action of a hexapole field on a ray parallel to the optic axis. If the ray enters the field, having a threefold symmetry, at a distance r from the optic axis, it experiences a small deflection proportional to r^2. Within a long hexapole field, the change of the distance to the optic axis has to be considered as well, which introduces a very small additional deflection of the ray proportional to r^3. A pair of rays at opposite sides $\boldsymbol{r}$ and $-\boldsymbol{r}$ to the optic axis will be deflected proportional to r^2 in the same direction, due to the threefold symmetry of the field, but small deflections proportional to r^3 point to opposite directions. Figure 2 displays ray diagrams for deflection by short and long hexapole fields. The net action of a hexapole field on a bundle of rays, each with distance r to the optic axis, is then a small divergence between rays at opposite sides to the axis, but at the cost of strong threefold distortion of the whole ray bundle. In the picture of ray aberrations, the threefold deflection represents a threefold astigmatism, and the divergence is negative spherical aberration. Figure 3 displays the corresponding ray displacements in the hexapole exit plane.

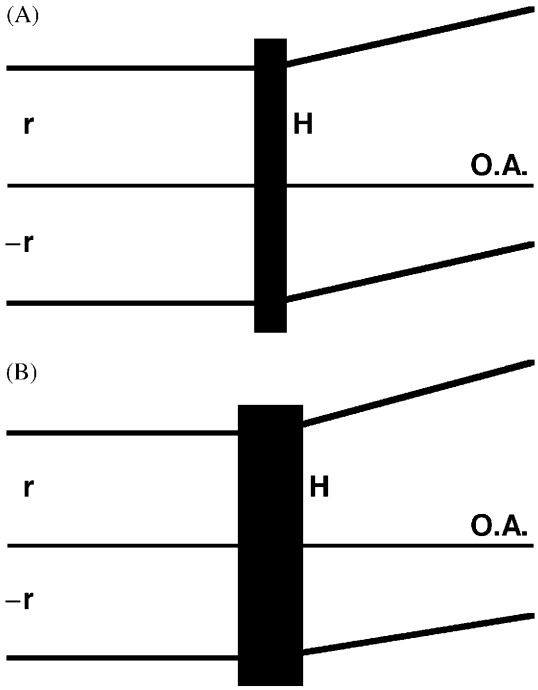

Figure 2. Ray paths through a hexapole field H for a pair of rays parallel to the optical axis $O.A$. The rays enter the field at distances $\boldsymbol{r}$ and $-\boldsymbol{r}$ in a dipole plane. **A:** Deflection through a short hexapole field proportional to r^2. **B:** Deflection proportional to r^2 and additional divergence proportional to r^3 through a long hexapole field.

The key idea of spherical aberration correction by a double hexapole is now the combination of two hexapole fields, so that the strong threefold distortions cancel and the two diverging deflections add. This is achieved by a transfer doublet of round lenses with a magnification of -1 between the two hexapole planes introducing a point inversion to the ray bundle. Another transfer doublet of round lenses is introduced between the objective lens of the microscope and the first hexapole plane. Its purpose is to image the coma-free point of the objective lens into the plane of the first hexapole. Thus the whole assembly of objective lens and corrector becomes semi-aplanatic, that is, off-axial aberrations are minimized, and a wide field of image points is spherical-aberration corrected (Rose, 1990). Figure 4 displays ray diagrams illustrating point inversion by the first transfer doublet and the deflection of a pair of rays by short and long hexapole fields.

The two hexapole elements are usually assembled as 12-poles to leave some freedom for the compensation of small relative misorientation of the two hexapole fields due to limited precision of the machining setup. For the same reason, a number of deflection coils is added in order to

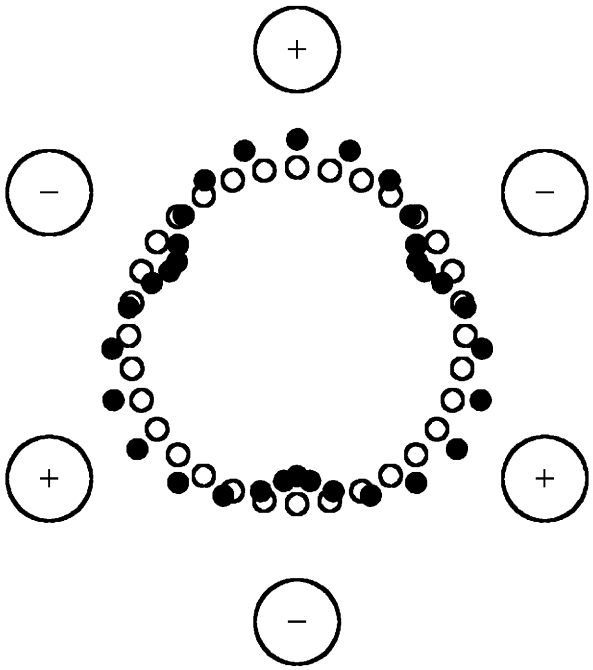

Figure 3. Distortion of a ray bundle through a hexapole field, with a view along the optical axis. The poles are marked by plus and minus signs, the rays before and after deflection by empty and filled circles, respectively.

match all optic axes of the single elements, the 12-pole elements, and the round lenses.

In the first feasibility stage of the project, the aberration corrector was installed on a test bench to demonstrate spherical aberration correction (Haider et al., 1995). The test setup consisted of a modified scanning electron microscope with the whole corrector incorporated into the specimen chamber and a CCD camera coupled to a scintillator on a viewing port beneath the specimen chamber. A small electron probe was focused on the scintillator, and through scanning the electron beam on circles with varying diameter, the ray displacements induced by the aberration corrector could be observed. With this procedure, the single corrector elements were trimmed and a good agreement of the electron optic properties with theory was shown.

In the second stage of the project, the aberration corrector was adapted to a commercial Philips CM 200 FEG ST (Haider et al., 1995, 1998*a*). The lower pole piece of the objective lens was modified to gain space for the first transfer lens of the corrector, and the vacuum system of the microscope was adapted to maintain high vacuum in the specimen area. Computer-controlled power supplies driving the currents through the various corrector elements were set up to provide a relative stability of around 10^{-5}. In addition, a so-called adapter lens was added between the aberration corrector and projector lenses of the microscope to maintain a parallel beam path within the corrector and to enable the operator to use the microscope controls as

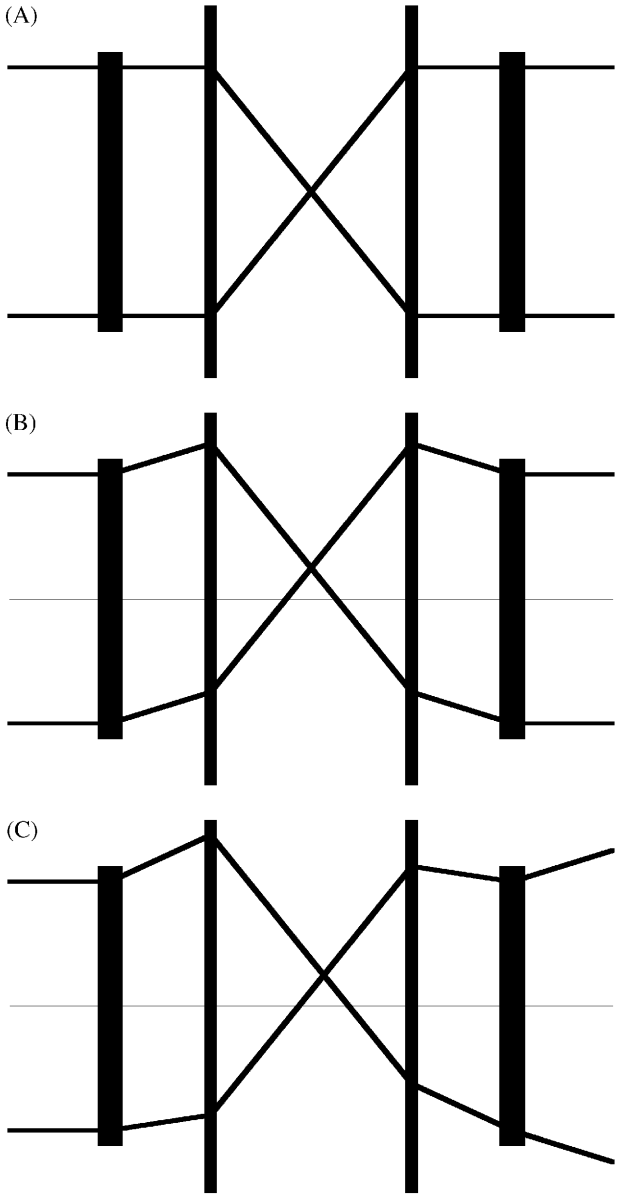

Figure 4. Operation modes of a double-hexapole corrector. The two elements in the center denote round lenses; the two elements to the left and right denote hexapole fields. **A:** Hexapoles switched off: A pair of rays, entering from the left, leaves the device undeflected, with a magnification of -1. **B:** Short Hexapole field: A pair of rays leaves the device undeflected, because the deflections of the two hexapole fields cancel. **C:** Long hexapole field: A pair of rays leaves the device with a pure divergence, because the two hexapole deflections cancel and the two divergences add up.

usual. Through integration of the aberration corrector, the chromatic aberration coefficient of the corrected microscope increased from a value of 1.3 mm for the uncorrected instrument to 1.7 mm. The resulting small deterioration of the information limit was compensated by decreasing the energy spread of the source to 0.7 eV FWHM, measured

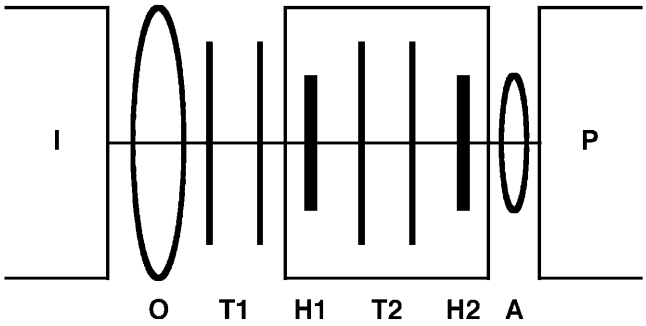

Figure 5. Integration of a double-hexapole corrector into a transmission electron microscope. The device, comprising the hexapole elements H1, H2 and the doublet of round lenses, T2, is inserted between the objective lens O and the projector system P of the microscope. A doublet of round lenses, T1, is used to image the coma-free point of the objective lens into the first hexapole plane. An additional lens A is used to adapt the whole ray path to the projector system. The illumination system, I, of the microscope is unchanged.

using an electron energy-loss spectrometer, due to reduction of the temperature of the field emission tip by 100 K. Figure 5 illustrates the integration of the double-hexapole corrector, its transfer lenses, and the adapter lens between the objective lens and the projector system of the microscope.

Aberration Measurement and Corrector Alignment

The double-hexapole aberration corrector provides a number of ways to compensate for the aberrations of the whole imaging system of the microscope, in particular the objective lens, through the excitation of deflectors, lenses, and the various coils of the 12-poles. The corresponding currents can be adjusted within wide limits, and the actual current settings are dependent on precise aberration measurement (Uhlemann & Haider, 1998).

The measurement is carried out by recording a Zemlin tableau of diffractograms (Zemlin et al., 1978; Typke & Dierksen, 1995) from an amorphous specimen area. Through a series of diffractograms with intentional illumination tilts, information on the true aberrations of the imaging system is collected by measuring the individual induced first-order aberrations of defocus and twofold astigmatism. The lens defocus is set to a certain underfocus prior to the measurement to generate Thon rings, which are then compared, diffractogram by diffractogram, with a database of Thon ring patterns for a wide range of defocus and twofold astigmatism (Uhlemann & Haider, 1998). The measured set of induced defocus and twofold astigmatism enters, together with the known illumination tilts, a set of linear equations for the desired true lens aberrations. Finally, the solution for the true lens aberrations is translated via a calibration table to lens current values for the individual corrector elements (Uhlemann & Haider, 1998). The whole measurement procedure runs on a separate computer driving the camera and the illumination system of the microscope via remote control. The microscope operator finally decides on the basis of the displayed aberration analysis to correct the individual aberrations via push buttons. An additional feature of the control software is a push button for small intentional changes of the third-order spherical aberration.

The guide for the operator about which aberrations must be corrected and which aberrations are unimportant is the $\pi/4$ criterion: To keep the wave aberration, that is, the deviation from a wanted reference, within bounds, the magnitude of each single lens aberration should not cause a phase change of larger than $\pi/4$ at the information limit of the instrument (see, e.g., the table in Uhlemann & Haider, 1998). It is appreciated that this rule is only approximate and may not reflect the state of the whole aberration function, which is the sum of all individual aberration contributions: On the one hand, single aberrations of the same symmetry violating the $\pi/4$ criterion may cancel favorably if they have different sign, such as a small positive third-order spherical aberration and a small underfocus, or a small positive twofold astigmatism and a small negative third-order star aberration with the same azimuth. On the other hand, such aberrations might well add up to exceed jointly the $\pi/4$ phase change at the information limit. To aid the operator and to give an overview of the state of the whole aberration function, the corresponding phase plate is displayed by the control software as a contour map together with the $\pi/4$ contour.

Contrast Transfer and New Imaging Modes

In traditional high-resolution electron microscopy, the fixed large value of the third-order spherical aberration imposes limits to the contrast transfer of thin objects. For modern midvoltage microscopes, the Scherzer point resolution is lower than the information limit, which is determined by the temporal coherence of the electron source. At Lichte's defocus of least confusion, contrast reversals still occur, making high-resolution structure interpretation difficult, and at the minimum phase-contrast setting, the defocus aberration and the spherical aberration do not cancel properly at higher spatial frequencies.

With the added freedom of variable spherical aberration, the above three important imaging modes can be optimized (Lentzen et al., 2002). For perfect aberration correction, zero defocus, and zero spherical aberration, the phase contrast of a thin object vanishes. Because the aberration function is zero, its gradient and therefore all ray

displacements vanish as well, leaving a contrast delocalization of zero. In this imaging mode, the point spread in the imaging plane is given by the information limit alone. The image intensity is given by

$$I(\boldsymbol{r}) = |\psi(\boldsymbol{r}) * p(\boldsymbol{r})|^2, \tag{10}$$

where $\psi(\boldsymbol{r})$ is the exit wave function and $p(\boldsymbol{r})$ is the point-spread function of the objective aperture or the virtual aperture originating from the partial coherence of the illuminating electron wave. The resulting amplitude contrast is not perceptible for very thin specimens, but if the specimen thickness increases, then modulations of the electron intensity become visible. The intensity modulation is particularly strong for a crystalline object viewed along a low-index crystal axis, where the intercolumn distances are well resolved and the intensity maxima resemble the atomic column positions. In simple crystal structures, such as Ge [110], the excitation of scattered waves is large at odd multiples of the extinction distances, and the atomic amplitude contrast also takes a maximum (Lentzen et al., 2002). Hence, perfect aberration correction comprises three properties: vanishing contrast from a weak-phase object, vanishing delocalization, and strong amplitude contrast.

If the corrected microscope is aligned for a spherical aberration of zero, positive phase contrast of a weak-phase object can still be obtained by the defocus aberration alone:

$$Z_0 = -(\lambda g_{\max}^2)^{-1} \tag{11}$$

provides a pass band up to the information limit $g_{\max}$, at a delocalization of $R_0 = 1/g_{\max}$.

Positive phase contrast from a weak-phase object can be optimized with the aberration corrector by extending Scherzer's point resolution to the information limit. Using $g_{\mathrm{Sch}} = g_{\max}$ and solving for the spherical aberration C_{30} yields (Lentzen et al., 2002)

$$C_{30,\mathrm{Sch}} = 16/(3\lambda^3 g_{\max}^4) \tag{12}$$

with the corresponding defocus

$$Z_{\mathrm{Sch}} = -8/(3\lambda g_{\max}^2). \tag{13}$$

The resulting delocalisation is $R_{\mathrm{Sch}} = 8/(3g_{\max})$, and the atomic object structure is visible as dark contrast relative to the background. Similar expressions were derived by O'Keefe (2000) starting with the defocus condition $Z = -(C_S\lambda)^{1/2}$ instead of (4), and an old calculation by Scherzer (1970) includes further the resolution limit possibly imposed by the fifth-order spherical aberration C_{50}. It is immediately clear that setting (12) and (13) has an unfavorable relation of blur due to the information limit and blur due to the delocalization. The latter is almost three times as large as the information limit!

Therefore, a better aberration setting has to be found that maintains strong positive phase contrast and reduces delocalization. This compromise can be achieved by equating Scherzer's defocus and Lichte's defocus of least confusion, $Z_{\mathrm{Sch}} = Z_{\mathrm{L}}$, and solving for the spherical aberration (Lentzen et al., 2002):

$$C_{30,\mathrm{opt}} = 64/(27\lambda^3 g_{\max}^4) \tag{14}$$

with the corresponding defocus

$$Z_{\mathrm{opt}} = -16/(9\lambda g_{\max}^2). \tag{15}$$

The amount of delocalization is $R_{\mathrm{opt}} = 16/(27g_{\max})$, which is 9/2 times smaller than for the Scherzer pass band extended to the information limit. Numerical analysis shows that the phase contrast is reduced by only 10% with this optimum setting for the corrected Philips CM200 (Lentzen et al., 2002). Figure 1D–E displays the phase contrast transfer functions for the extended phase contrast and the extended phase contrast with reduced delocalization. Table 1 gives the corresponding settings for defocus and spherical aberration, as well as the resulting values for delocalization in the image plane.

The above considerations have shown how the new freedom of variable spherical aberration can be exploited to optimize the imaging mode used in traditional high-resolution investigations, namely the important pass-band imaging of very thin weak-phase objects. The large fixed spherical aberration is always positive for traditional transmission electron microscopes. Thus, the only way to produce phase contrast from a thin object is to use an underfocus setting. The resulting aberration function is negative for Scherzer pass-band imaging, and the phase change is positive. The positive phase contrast from a weak-phase object is therefore dark relative to the mean intensity, and crystalline regions of a thin object show dark-atom contrast.

The variable spherical aberration offers, besides optimizing positive phase contrast, access to negative phase contrast as well. This is achieved by reversing all aberrations, that is, to use negative spherical aberration combined with overfocus (Lentzen et al., 2002). The values are then the same as before, for the extended Scherzer pass band and the optimized pass band with reduced delocalization, but with all signs reversed. The resulting aberration function is then positive for the pass band imaging, and the phase change is negative. For very thin weak-phase objects, the negative phase contrast is therefore bright relative to the mean intensity; crystalline regions of a thin object show bright-atom contrast. Figure 1E,F displays the phase contrast transfer functions for positive and negative spherical aberration.

The traditional imaging mode with positive spherical aberration combined with underfocus and the new imaging mode with negative spherical aberration and overfocus pro-

duce within linear imaging theory an atom contrast being symmetrical with respect to the mean intensity (Lentzen et al., 2002). If nonlinear contrast contributions are considered, however, then a striking asymmetry occurs. The new imaging mode produces stronger contrast modulation at atom column sites than the traditional imaging mode. This asymmetry has been investigated by image simulations for a number of crystal structures (Jia et al., 2004), because an analytical treatment invoking the full imaging formalism using the transmission cross-coefficients for partially coherent illumination is very complicated and gives no simple picture of the underlying contrast mechanism.

A simple picture can be gained, however, if an ideal Zernike phase plate is assumed for both imaging modes (Jia et al., 2004), that is, transmission of the direct, unscattered wave ψ_0 with a coefficient of 1 and transmission of the scattered wave $\psi_{sc}(\boldsymbol{r}) = \pi i \lambda U(\boldsymbol{r}) t$ with a coefficient of $+i$ for positive phase contrast and $-i$ for negative phase contrast. Here $U(\boldsymbol{r})$ denotes the projected crystal potential and t the specimen thickness. The exit wave in the object plane,

$$\psi_{obj}(\boldsymbol{r}) = \psi_0 + \pi i \lambda U(\boldsymbol{r}) t, \tag{16}$$

is altered by the phase plate to the exit wave in the imaging plane,

$$\psi_{im}(\boldsymbol{g}) = \psi_0 \mp \pi \lambda U(\boldsymbol{r}) t, \tag{17}$$

and the resulting image intensity to second order in $U(\boldsymbol{r})$ is

$$I(\boldsymbol{r}) = \psi_0^2 \mp 2\pi\psi_0 \lambda U(\boldsymbol{r}) t + (\pi \lambda U(\boldsymbol{r}) t)^2. \tag{18}$$

The upper sign holds for positive phase contrast, the lower sign for negative phase contrast, and a common phase of ψ_0 and $\psi_{sc}(\boldsymbol{r})$ has been chosen to set ψ_0 to a real value. Figure 6 displays the intensity traces across an atom column site.

The comparison of both cases shows that the linear contribution and the quadratic contribution have a different sign for positive phase contrast. The local intensity modulation at an atom colum site is weak, because the linear modulation is partially cancelled by the nonlinear modulation. The linear contribution and the quadratic contribution have the same sign for negative phase contrast. The local intensity modulation at an atom column site is strong, because linear modulation and nonlinear modulation reinforce each other. In other words, using negative spherical aberration combined with overfocus enhances the atomic contrast from thin specimens compared to a setting with positive spherical aberration and underfocus.

The above considerations have treated the case of thin samples, where the scattered wave has only a small modulation relative to the direct, transmitted wave, and where single scattering by the projected crystal potential within the first Born approximation leads to a phase of the scattered wave of $\pi/2$ relative to the direct wave. This restricts,

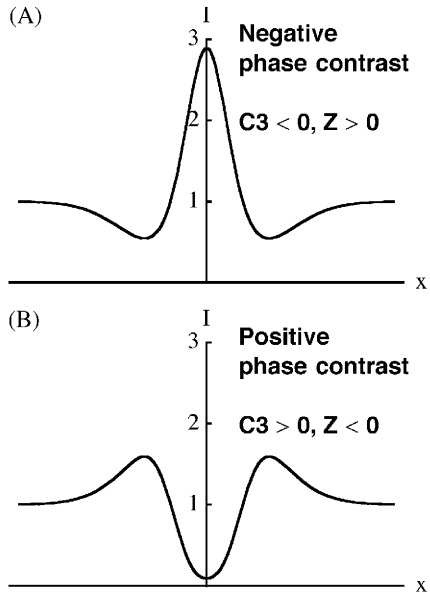

Figure 6. Intensity distribution at a single atom column with bright-atom and dark-atom contrast. **A:** Imaging with small negative spherical aberration, C_3, combined with a small overfocus, Z, provides negative phase contrast. **B:** Imaging with a small positive spherical aberration, C_3, combined with a small underfocus, Z, provides positive phase contrast.

in general, the calculation of an optimum contrast transfer of the electron microscope to unrealistically thin samples, that is, the projected crystal columns contain one heavy atom, at most, with large atomic number, or only a few light atoms with small atomic number. In materials science investigations, however, standard sample preparation techniques provide much thicker samples, with thicknesses on the order of a few nanometers and columns containing more than one heavy atom or a larger number of light atoms.

For thicker crystalline samples viewed along a low-index orientation, the scattered electron wave still has a local modulation resembling the projected column positions. At electron energies of 200–300 keV and for atoms with small or medium atomic numbers, the local modulation of the scattered electron wave can be described by the superposition of two eigenstates of electron channeling, which leads to characteristic beating with a thickness period equal to the extinction distance ξ (Kambe et al., 1974; Fujimoto, 1978). The direct electron wave can be described by

$$\psi_0 = \cos(\pi z/\xi) + i(U_0 \lambda \xi - 1)\sin(\pi z/\xi) \tag{19}$$

and the scattered wave by

$$\psi_{sc}(\boldsymbol{r}) = i(U(\boldsymbol{r}) - U_0)\lambda\xi \sin(\pi z/\xi), \tag{20}$$

with the specimen thickness z and the mean projected crystal potential U_0 (Lentzen & Urban, 2000).

The striking property of the electron wave at larger specimen thickness is that the modulation of the scattered wave is still proportional to the projected crystal potential, but its phase relative to the direct wave deviates from $\pi/2$. Depending on the strength of the scattering, that is, depending on the projected atomic charge per unit length along the crystal column, the relative phase starts at $\pi/2$ and increases steadily, if $U_0\lambda\xi < 1$. It starts at $\pi/2$ and decreases steadily, if $U_0\lambda\xi > 1$.

In light of the above calculations on the optimum Zernike phase plate for bright-atom imaging, enhancing the intensity modulation at the atomic column sites, it is clear that the optimum compensating phase, $-2\pi\chi_0$, of the Zernike phase plate for thicker samples is dependent on the properties of electron channeling, namely, the specimen thickness z, the extinction distance ξ, and the mean projected crystal potential U_0. A detailed calculation (Lentzen, 2004) yields two important equations:

$$\tan(2\pi\chi_0) = ((U_0\lambda\xi - 1)\tan(\pi z/\xi))^{-1} \tag{21}$$

and

$$\tan(\pi z/\xi)\sin(2\pi\chi_0) > 0. \tag{22}$$

The first has to be solved for the compensating aberration χ_0, and the second determines which of the solutions in the interval $-\frac{1}{2} < \chi_0 < \frac{1}{2}$ is then selected to determine the optimum setting for defocus,

$$Z_{\text{opt}} = 8\chi_0/(\lambda g_{\max}^2), \tag{23}$$

and spherical aberration,

$$C_{30,\text{opt}} = -40\chi_0/(3\lambda^3 g_{\max}^4). \tag{24}$$

The phase plate approximates an optimum Zernike phase plate for bright-atom contrast from a thicker sample; its delocalization is

$$R_{\text{opt}} = 16|\chi_0|/(3g_{\max}), \tag{25}$$

and the image intensity of a single atom column becomes

$$I(\boldsymbol{r}) = ((\cos^2(\pi z/\xi) + (U_0\lambda\xi - 1)^2\sin^2(\pi z/\xi))^{1/2} + (U(r) - U_0)\lambda\xi|\sin(\pi z/\xi)|)^2, \tag{26}$$

under the simplified assumption of coherent illumination.

The optimum aberration settings for a thicker crystal were confirmed through a numerical study including the effects of partially coherent illumination by using image simulations of Ge[110] (Lentzen, 2004). The study showed that the intensity modulation at the atom column sites is enhanced, as expected, but also that problems may arise if the scattered wave already has strong modulation, for example, at specimen thicknesses close to half the extinction distance. Then "ghost intensity" may appear at the tunnel position between the Ge columns, which is unrelated to the projected structure.

The equations for optimum defocus and spherical aberrations show that neither positive nor negative spherical aberration is alone important for imaging in real materials science investigations, but an interval from -100 to 100 μm at 200 kV is preferred. The thickness variation of the sample requires an adaptation of the aberration function from positive to negative values.

Practical Aspects

The above sections have shown how an aberration corrector can be used in several ways in transmission electron microscopy to optimize the high-resolution imaging of objects in materials science investigations. An overview of the principle of aberration measurement, aberration correction, and the beneficial use of certain defocus and spherical aberration settings have been described. It has been assumed that measurements and corrections work perfectly, and that the operator desire for a specific aberration setting can be executed precisely. This final section is dedicated to practical aspects.

The prerequisite of precise aberration measurement via the evaluation of a Zemlin tableau is an accurate determination of defocus and twofold astigmatism from single diffractograms. The thin amorphous specimen areas used to record diffractograms must exhibit a constant defocus over the field of view, that is, a flat exit face. Otherwise, the defocus change induced, for example, by an inclined or uneven specimen would introduce a respective defocus spread attenuating the Thon ring pattern and deteriorate the high-frequency information needed for precise measurement. A similar condition applies for the thickness of the amorphous thin film: Scattering from atoms at the top face is related to a different focus plane than scattering from atoms at the bottom face. The defocus spread introduced by contributions from both faces and planes inside the sample can be determined from the fall-off of the kinematical envelope sinc πst, with $s = \frac{1}{2}\lambda g^2$ (see, e.g., Hirsch et al., 1967) to a value of $2/\pi$, in the framework of single scattering. The upper limit to the thickness of the amorphous film, $t_{\max}$, is then equal to the spread:

$$t_{\max} = 1/(\lambda g_{\max}^2). \tag{27}$$

A third condition for precise measurement is a large enough extension of the amorphous material in real space to avoid a

blur in reciprocal space. Thin stripes of amorphous material, for example, produce characteristic streaks in reciprocal space, which may bias the search for the appropriate defocus and astigmatism when evaluating a diffractogram.

All these conditions can be met by using special test samples, such as a very thin amorphous tungsten film evaporated on a very thin carbon film. In many materials science investigations, however, one has to work with the thin amorphous material left by sample preparation, which may sometimes be too thick or exhibit only thin stripes.

Using an aberration corrector for high-resolution imaging permits the use of a larger convergence angle of the illumination than is used in an uncorrected instrument (Haider et al., 1998*a*). A small amount of residual lens aberrations is linked to very small gradients of the aberration function. The convergence and the gradient of the aberration function enter the spatial coherence envelope as a product, and therefore two aspects follow for high-resolution imaging. First, a larger amount of electrons can be collected from the source by using larger convergence without affecting spatial coherence. The specimen can be illuminated with a higher intensity, and shorter exposure times can be used. In modern high-resolution instruments equipped with field-emission guns, however, exposure times are already short, on the order of a second or below. Second, the new freedom of higher convergence can be used instead to move the illumination crossover away from the specimen plane and to return to traditional exposure times on the order of one second. Because the crossover has been moved, the outer parts of the field of view are less affected by illumination tilt, which may affect strongly the direct interpretation of structure details in crystalline samples.

If aberrations are corrected perfectly, then illumination tilt will not induce further aberrations, like induced aberrations due to the strong spherical aberration in an uncorrected instrument (Haider et al., 1998*a*). Illumination tilt can now be used to compensate global specimen tilt, which is particularly useful for work with crystalline samples, which require exact orientation of atom columns parallel to the electron beam. In almost every case, however, aberrations cannot be compensated perfectly, as follows already from the limited accuracy of aberration measurements. The measurement routines permit aberrations to just fulfill the $\pi/4$ criterion, that is, the area in reciprocal space given by the information limit of the instrument is just corrected, but the area beyond the information limit is not. Introducing illumination tilt is equivalent to a shift in reciprocal space: One part of the well-corrected area moves outside, another part of the uncorrected area moves inside the area used for imaging. From this consideration it is clear that the specimen tilt compensation can only be used for low-resolution work, where the low resolution plus the illumination tilt used do not exceed the radius of the aberration-corrected area.

Calculations for contrast transfer and certain imaging modes always assume a flat specimen; that is, only one object plane, usually the exit plane, is of interest for various kinds of ideal imaging. Real objects often have shapes deviating considerably from this condition. Two important examples are the inclined bottom face of a wedge-shaped specimen and the uneven exit face of a particle on a thin support (see Fig. 7). The sites for any optimum defocus are given by the intersection of the specimen shape and the respective plane used for optimum imaging. It is immediately clear that the need for optimum imaging of all sites of an uneven exit face compels the recording of a through-focal series of images (Lentzen et al., 2002). Such a series can be exploited in two ways: First, an optimum image of a special specimen location of interest can be selected after the experiment without the need for exact focusing during the microscope session. Second, a defocus series of images can be used to reconstruct the exit-wave function over the whole field of view (Schiske, 1968; Saxton, 1988; Coene et al., 1992, 1996; Thust et al., 1996*a*). Valuable structural information can be gained by improving the aberration setting of the microscope after the experiment through numerical aberration correction of the exit-wave function (Thust et al., 1996*b*; Lehmann, 2000; Saxton, 2000). Another benefit is the freedom to change the wave function numerically by defocus phase plates. These give access to focus planes that were not sampled by the image series, and thus very accurate optimum defocus settings can be made after the experiment.

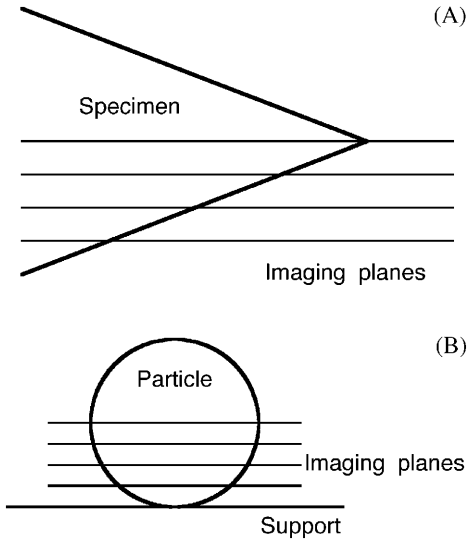

Figure 7. Defocus series for objects with uneven bottom surfaces. **A:** Wedge-shaped specimen. **B:** Particle on a support film.

In certain cases, aberration correction can be used to apply two different imaging modes simultaneously. If the specimen contains two planes of interest perpendicular to the electron beam, then perfect aberration correction, that is, zero spherical aberration and zero defocus, can be used to make the weak contrast due to atoms in one plane vanish

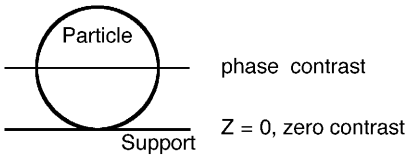

Figure 8. Simultaneous use of two imaging modes for a particle on a thin support film. For zero spherical aberration and zero defocus with respect to the support film the phase contrast from the particle is not disturbed by contrast from the support.

and to allow the other plane to be in contrast through the defocus aberration equivalent to the distance between planes. For example, the atomic structure of small crystalline particles on a thin amorphous support film can be studied without disturbing contrast due to the film if zero defocus is applied for the film plane. Then the particle yields phase contrast through the amount of defocus related to its thickness (see Fig. 8).

Materials Science Applications

The aberration-corrected Philips CM 200 FEG, equipped with the Rose–Haider double hexapole corrector, was transferred from the EMBL Heidelberg to the Research Centre Jülich in 1997. A series of articles document the state of the project at the beginning of the materials science application of the instrument (Haider et al., 1998*a*, 1998*b*, 1998*c*; Uhlemann & Haider, 1998; Urban et al., 1999). The key result at this stage was the demonstration of spherical-aberration correction with an information limit of 0.12 nm in the direction of the long axis of a single-tilt holder and 0.14 in the perpendicular direction. At the same time, two materials science investigations demonstrated the use of the corrected instrument for high-resolution structure investigations: the structure image of a GaAs crystal viewed along the [110] zone axis and the structure image of a $Si/CoSi_2$ interface with and without aberrations corrected (Haider et al., 1998*a*, 1998*b*). The latter example showed the very small delocalization of aberration-corrected imaging compared with the large delocalization at the original value of the spherical aberration of 1.23 mm.

After a number of improvements of the installation at Research Centre Jülich, an information limit of better than 0.13 nm was reached (Lentzen et al., 2002). High-resolution investigations were carried out in several materials systems: thin layers of AlSb embedded in GaSb, a GaAs/AlAs/GaAs hetero-structure, a tilt grain boundary in a $Ba_{0.7}Sr_{0.3}TiO_3$ thin film, and grains and grain boundaries in a $Ba_{0.7}Sr_{0.3}TiO_3$ thin film (Lentzen et al., 2002). The latter material was chosen to image all types of atomic columns in the [110] projection of $Ba_{0.7}Sr_{0.3}TiO_3$, including the weakly scattering oxygen columns close to Ti–O columns.

Further work was dedicated to the investigation of optimum imaging of weakly scattering atom columns in the vicinity of strongly scattering columns (Jia et al., 2003, 2004; Jia & Urban, 2004). As described above in the section on contrast transfer and new imaging modes, imaging with a positive aberration function, that is, negative phase contrast with negative spherical aberration and overfocus, is well suited to enhance the image contrast of very thin specimens. In a thin specimen of $SrTiO_3$ all atomic columns could be resolved, in particular the weakly scattering oxygen columns. By comparison with image simulations, it was confirmed that the image intensity at the oxygen columns varies almost linearly with the oxygen occupancy, and this calibration was then used to measure oxygen content at individual sites. Using the oxygen sublattice as a fingerprint, details of the core structure of two different types of edge dislocations in $SrTiO_3$ were investigated. Negative phase contrast was further used to image a stacking fault in $YBa_2Cu_3O_7$ with thin films viewed along the [100] and the [010] directions. In both directions, all types of atom columns were resolved, and a translation of the two crystals between the double copper-oxide chain planes by one-half of the (010) lattice parameter could be observed. The structural information could be used to identify the stacking fault as a 124 type. A close look at the intensity related to the oxygen column positions in the two projections revealed strong oxygen ordering in the copper-oxide double plane. Another application of negative phase contrast has been the measurement of the oxygen occupancy at the $\Sigma 3$ {111} twin boundaries of a $BaTiO_3$ thin film (Jia & Urban, 2004). Figure 9 displays a high-resolution image of the thin film recorded under negative phase contrast conditions. The observed average oxygen deficiency of 32% at the twin boundary sites was explained by the reduction of the grain boundary energy through a modified Ti_2O_9 group, providing a way to accommodate oxygen vacancies in this oxygen-deficient material by the formation of a nanotwin lamellae structure.

Work on defects in GaAs concentrated on the measurement of lattice distortions around dislocations and on investigation of the dislocation core structure (Tillmann et al., 2004). A high-resolution image under optimum negative phase-contrast conditions was compared to the phase of the exit-wave function reconstructed from a defocus series of images. The negative phase contrast image of a multiple stacking fault terminated by partial dislocations revealed a high-resolution view of the atomic columns, but was disturbed by ghost intensity at the tunnel positions of GaAs [110]. The phase of the reconstructed exit-wave function provided a clearer view, chiefly for three reasons: First, the information from the image series is less affected by noise due to amorphous layers, because the reconstruction algorithm extracts an average. Second, the image directly resembles the structure, because the ghost intensity at the tunnel positions is absent. Third, the fine-tuning of residual aberrations, by numerical aberration correction after the exper-

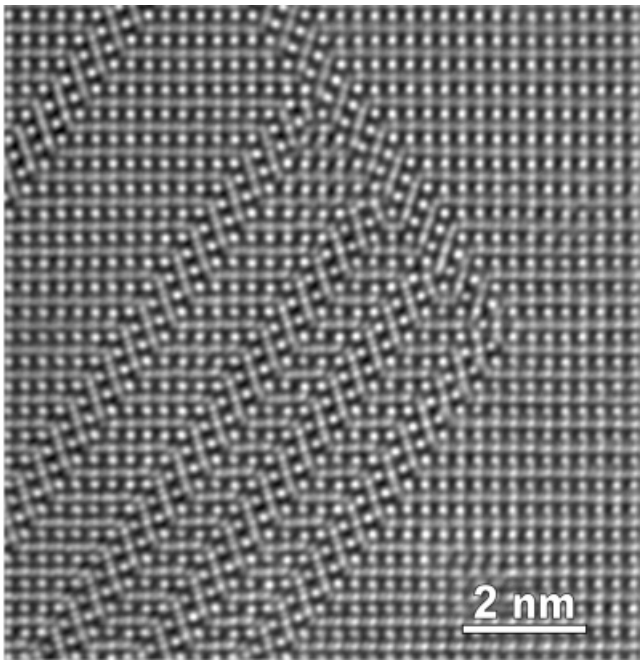

Figure 9. High-resolution image of the atomic structure of a $BaTiO_3$ [011] thin film containing twin lamellae, recorded under negative phase contrast conditions due to a small negative spherical aberration combined with a small overfocus. All atom columns, Ba, Ti-O, and O, appear bright with respect to the mean intensity (from the work presented in Jia & Urban, 2004).

iment, eliminates any residual delocalization, in particular delocalization due to the Scherzer phase plate needed for optimum imaging.

Outlook

In recent years, the major manufacturers of transmission electron microscopes have started to integrate aberration correctors, all of the double-hexapole type, into their instruments. The objective is not only to make aberration correction and aberration control available for materials science, but also to improve the information limit of medium-voltage instruments substantially, into the region of sub-Ångström resolution. Meanwhile, new instruments with an aberration-corrected objective lens have been installed, one at Oxford University and another at the University of Nagoya. The instrument at Oxford has been used for high-resolution investigations of a niobium oxide crystal, CdSe nano particles, Si [110], and the oxy-fluoride $6Nb_2O_5 \cdot FeF_3$ (Hutchison et al., 2002; Kirkland et al., 2004); the instrument at Nagoya has been used for high-resolution investigations of SiO_2/Si(110) interfaces and InGaAs dots embedded in GaP (Hosokawa et al., 2003; Tanaka et al., 2003, 2004). Two more aberration-corrected instruments have been installed at CEMES, Toulouse, and at the Triebenberg Laboratory, Dresden, with first results of the latter instrument obtained with high-resolution electron holography of a GaAs crystal (Lehmann et al., 2005).

Calculations, dating back to Scherzer's article of 1949, show that optimum phase contrast imaging for sub-Ångström resolution will be limited by the fifth-order spherical aberration (Scherzer, 1970). Its coefficient is positive, and optimum imaging will thus require the combination of positive fifth-order aberration with negative third-order spherical aberration and overfocus.

Many more aberration coefficients will have to be measured in the future, which will be possible with improved measurement routines. The precise tuning of a proper defocus may, however, be difficult, because of uneven specimen surfaces and other experimental insufficiencies that require the recording of through-focus series for materials science investigations. In our view, the combination of hardware aberration correction, giving a direct view at the structure under investigation through optimum phase contrast imaging, and numerical aberration correction through exit-wave reconstruction techniques will pave the way to materials science investigations that exploit the very instrumental limits.

Conclusions

More than 60 years after the invention of the electron microscope, the design and construction of the double-hexapole aberration corrector has made it possible to construct the prototype of a spherical-aberration corrected transmission electron microscope dedicated to high-resolution imaging on the atomic scale. The key feature of the corrected instrument, a Philips CM200 FEG ST, is an information limit of better than 0.13 nm and the possibility to vary the spherical aberration within wide limits, even to negative values. The aberration measurement and the corrector control provide instrument alignments that turned out to be stable enough for materials science investigations.

Analysis of the contrast transfer with the new possibility of a tunable spherical aberration has revealed new imaging modes: high-resolution amplitude contrast, extension of the point resolution to the information limit, and enhanced image intensity modulation for negative phase contrast. In particular, the latter mode provides through the combination of a small negative spherical aberration and a small overfocus the high-resolution imaging of weakly scattering atom columns, such as oxygen, in the vicinity of strongly scattering atom columns.

Acknowledgments

The author thanks all coworkers in the project on aberration correction of a transmission electron microscope, in

particular M. Haider, Heidelberg, H. Rose, Darmstadt, and K. Urban, Jülich, for the many discussions on electron optics and aberration correction, the opportunity to work in this exciting field, support during the past years, and encouragement in compiling this work. M.L. thanks further C.L. Jia, A. Thust, B. Kabius, E. Schwan, K. Tillmann, and B. Jahnen for collaboration on methods and materials science applications of aberration correction and extensive support with the aberration-corrected prototype. The project on aberration correction was funded by the Volkswagen Stiftung.

References

Bastian, B., Spengler, K. & Typke, D. (1971). An electric-magnetic octopole element to correct spherical and chromatical aberrations of electron lenses. *Optik* **33**, 591–596.

Batson, P.E., Dellby, N. & Krivanek, O.L. (2002). Sub-Angstrom resolution using aberration corrected electron optics. *Nature* **418**, 617–620.

Beck, V.D. (1979). A hexapole spherical aberration corrector. *Optik* **53**, 241–255.

Bernhard, W. (1980). Erprobung eines sphärisch und chromatisch korrigierten Elektronenmikroskops. *Optik* **57**, 73–94.

Born, M. & Wolf, E. (1980). *Principles of Optics*. Cambridge: Cambridge University Press.

Coene, W. & Jansen, A.J.E.M. (1992). Image delocalisation and high resolution transmission electron microscopic imaging with a field emission gun. *Scan Microsc* **6**(Suppl.), 379–403.

Coene, W., Janssen, G., Op de Beeck, M. & Van Dyck, D. (1992). Phase retrieval through focus variation for ultra-resolution in field-emission transmission electron microscopy. *Phys Rev Lett* **69**, 3743–3746.

Coene, W.M.J., Thust, A., Op de Beeck, M. & Van Dyck, D. (1996). Maximum-likelihood method for focus-variation image reconstruction in high resolution transmission electron microscopy. *Ultramicroscopy* **64**, 109–135.

Dellby, N., Krivanek, O.L., Nellist, P.D., Batson, P.E. & Lupini, A.R. (2001). Progress in aberration-corrected scanning transmission electron microscopy. *J Microsc* **50**, 177–185.

Eisenhandler, C.B. & Siegel, B.M. (1966). Imaging of single atoms with the electron microscope by phase contrast. *J Appl Phys* **37**, 1613–1619.

Fey, G. (1980). Electric power supply for an electron-optical corrector. *Optik* **55**, 55–65.

Fujimoto, F. (1978). Periodicity of crystal structure images in electron microscopy with crystal thickness. *Phys Status Solidi A* **45**, 99–106.

Gabor, D. (1949). Microscopy by reconstructed wave-fronts. *Proc Roy Soc A* **197**, 454–487.

Haider, M., Braunshausen, G. & Schwan E. (1995). Correction of the spherical aberration of a 200 kV TEM by means of a Hexapole-corrector. *Optik* **99**, 167–179.

Haider, M., Rose, H., Uhlemann, S., Kabius, B. & Urban, K. (1998*a*). Towards 0.1 nm resolution with the first spherically corrected transmission electron microscope. *J Elect Microsc* **47**, 395–405.

Haider, M., Rose, H., Uhlemann, S., Schwan, E., Kabius, B. & Urban, K. (1998*b*). A spherical-aberration-corrected 200 kV transmission electron microscope. *Ultramicroscopy* **75**, 53–60.

Haider, M., Uhlemann, S., Schwan, E., Rose, H., Kabius, B. & Urban, K. (1998*c*). Electron microscopy image enhanced. *Nature* **392**, 768–769.

Heinemann, K. (1971). In-situ measurement of objective lens data of a high-resolution electron microscope. *Optik* **34**, 113–128.

Heinzerling, J. (1976). A magnetic flux stabilizer for the objective lens of a corrected electron microscope. *J Phys E* **9**, 131–134.

Hely, H. (1982*a*). Messungen an einem verbesserten korrigierten Elektronenmikroskop. *Optik* **60**, 353–370.

Hely, H. (1982*b*). Technologische Voraussetzungen für die Verbesserung der Korrektur von Elektronenlinsen. *Optik* **60**, 307–326.

Hirsch, P., Howie, A., Nicholson, R., Pashley, D.W. & Whelan, M.J. (1967). *Electron Microscopy of Thin Crystals*. London: Butterworths.

Hosokawa, F., Tomita, T., Naruse, M., Honda, T., Hartel, P. & Haider, M. (2003). A spherical aberration-corrected 200 kV TEM. *J Elect Microsc* **52**, 3–10.

Hutchison, J.L., Titchmarsh, J.M., Cockayne, D.J.H., Möbus, G., Hetherington, C.J.D., Doole, R.C., Hosokawa, F., Hartel, P. & Haider, M. (2002). A C_S corrected HRETM: Initial applications in materials science. *JEOL News* **37**E, 2–5.

Jia, C.L., Lentzen, M. & Urban, K. (2003). Atomic-resolution imaging of oxygen in perovskite ceramics. *Science* **299**, 870–873.

Jia, C.L., Lentzen, M. & Urban, K. (2004). High-resolution transmission electron microscopy using negative spherical aberration. *Microsc Microanal* **10**, 174–184.

Jia, C.L. & Urban, K. (2004). Atomic-resolution measurement of oxygen concentration in oxide materials. *Science* **303**, 2001–2004.

Kambe, K., Lehmpfuhl, G. & Fujimoto, G. (1974). Interpretation of electron channeling by the dynamical theory of electron diffraction. *Z Naturforsch A* **29**, 1034–1044.

Kirkland, A.I., Titchmarsh, J.M., Hutchison, J.L., Cockayne, D.J.H., Hetherington, C.J.D., Doole, R.C., Sawada, H., Haider, M. & Hartel, P. (2004). A double aberration corrected energy filtered HREM/STEM. *JEOL News* **39**, 2–5.

Kisielowski, C., Hetherington, C.J.D., Wang, Y.C., Kilaas, R., O'Keefe, M.A. & Thust, A. (2001). Imaging columns of the light elements carbon, nitrogen and oxygen with sub Ångstrom resolution. *Ultramicroscopy* **89**, 243–263.

Koops, H., Kuck, G. & Scherzer, O. (1976). Erprobung eines elektronenoptischen Aplanators. *Optik* **48**, 225–236.

Kuck, G. (1979). *Erprobung eines elektronenoptischen Korrektivs für Farb- und Öffnungsfehler*. Dissertation. Darmstadt: Technical University of Darmstadt.

Lehmann, M. (2000). Determination and correction of the coherent wave aberration from a single off-axis electron hologram by means of a genetic algorithm. *Ultramicroscopy* **85**, 165–182.

Lehmann, M., Geiger, D. & Lichte, H. (2005). First experiences using electron holography with a Cs-corrected TEM. *Microsc Microanal* **11**(Suppl. 2), 2146–2147.

Leith, E.N. & Upatnieks, J. (1962). Reconstructed wavefronts and communication theory. *J Opt Soc Am* **52**, 1123–1130.

Leith, E.N. & Upatnieks, J. (1963). Wavefront reconstruction with continuous-tone objects. *J Opt Soc Am* **53**, 1377–1381.

Leith, E.N. & Upatnieks, J. (1964). Wavefront reconstruction with diffused illumination and three-dimensional objects. *J Opt Soc Am* **54**, 1295–1301.

Lentzen, M. (2004). The tuning of a Zernike phase plate with defocus and variable spherical aberration and its use in HRTEM imaging. *Ultramicroscopy* **99**, 211–220.

Lentzen, M., Jahnen, B., Jia, C.L., Thust, A., Tillmann, K. & Urban, K. (2002). High-resolution imaging with an aberration-corrected transmission electron microscope. *Ultramicroscopy* **92**, 233–242.

Lentzen, M. & Urban, K. (2000). Reconstruction of the projected crystal potential in transmission electron microscopy by means of a maximum-likelihood refinement algorithm. *Acta Cryst A* **56**, 235–247.

Lichte, H. (1986). Electron holography approaching atomic resolution. *Ultramicroscopy* **20**, 293–304.

Lichte, H. (1991). Optimum focus for taking electron holograms. *Ultramicroscopy* **38**, 13–22.

O'Keefe, M.A. (2000). The optimum C_S condition for high-resolution transmission electron microscopy. *Microsc Microanal* **6**, 1036–1037.

O'Keefe, M.A., Hetherington, C.J.D., Wang, Y.C., Nelson, E.C., Turner, J.H., Kisielowski, C., Malm, J.-O., Mueller, R., Ringnalda, J., Pan, M. & Thust, A. (2001). Sub-ångstrom high-resolution transmission electron microscopy at 300 kV. *Ultramicroscopy* **89**, 215–241.

Rose, H. (1971). Elektronenoptische Aplanate. *Optik* **34**, 287–313.

Rose, H. (1990). Outline of a spherically corrected semiaplanatic medium-voltage transmission electron microscope. *Optik* **85**, 19–24.

Rose, H. (1994). Correction of aberrations, a promising means for improving the spatial and energy resolution of energy-filtering electron microscopes. *Ultramicroscopy* **56**, 11–25.

Saxton, W.O. (1978). *Computer Techniques for Image Processing in Electron Microscopy*. New York: Academic Press.

Saxton, W.O. (1988). Accurate atom positions from focal and tilted beam series of high resolution electron micrographs. In *Proceedings of the 6th Pfefferkorn Conference, Image and Signal Processing in Electron Microscopy*, Hawkes, P.W., Ottensmeyer, P.P., Saxton, W.O. & Rosenfeld, A. (Eds.), pp. 213–224. Chicago: Scanning Microscopy International.

Saxton, W.O. (1994). What is the focus variation method? Is it new? Is it direct? *Ultramicroscopy* **55**, 171–181.

Saxton, W.O. (2000). A new way of measuring microscope aberrations. *Ultramicroscopy* **81**, 41–45.

Scherzer, O. (1936). Über einige Fehler von Elektronenlinsen. *Z Phys* **101**, 593–603.

Scherzer, O. (1947). Sphärische und chromatische Korrektur von Elektronen-Linsen. *Optik* **2**, 114–132.

Scherzer, O. (1949). The theoretical resolution limit of the electron microscope. *J Appl Phys* **20**, 20–29.

Scherzer, O. (1970). Die Strahlenschädigung der Objekte als Grenze für die hochauflösende Elektronenmikroskopie. *Berichte der Bunsengesellschaft* **74**, 1154–1167.

Schiske, P. (1968). Zur Frage der Bildrekonstruktion durch Fokusreihen. In *Proceedings of the 4th Regional Congress on Electron Microscopy*, vol. 1, pp. 145–146. Rome, Italy: Tipografia Poliglotta Vaticana.

Schiske, P. (2002). Image reconstruction by means of focus series. *J Microsc* **207**, 154.

Tanaka, N., Yamasaki, J., Fuchi, S. & Takeda, Y. (2004). First observation of $In_xGa_{1-x}As$ quantum dots in GaP by spherical-aberration-corrected HRTEM in comparison with ADF-STEM and conventional HRTEM. *Microsc Microanal* **10**, 139–145.

Tanaka, N., Yamasaki, J., Usuda, K. & Ikarashi, N. (2003). First observation of SiO_2/Si(100) interfaces by spherical aberration-corrected high-resolution transmission electron microscopy. *J Elect Microsc* **52**, 69–73.

Thust, A., Coene, W.M.J., Op de Beeck, M. & Van Dyck, D. (1996*a*). Focal-series reconstruction in HRTEM: Simulation studies on non-periodic objects. *Ultramicroscopy* **64**, 211–230.

Thust, A., Overwijk, M.H.F., Coene, W.M.J. & Lentzen, M. (1996*b*). Numerical correction of lens aberrations in phase-retrieval HRTEM. *Ultramicroscopy* **64**, 249–264.

Tillmann, K., Thust, A. & Urban, K. (2004). Spherical aberration correction in tandem with exit-plane wave function reconstruction: Interlocking tools for the atomic scale imaging of lattice defects in GaAs. *Microsc Microanal* **10**, 185–198.

Tonomura, A. (1993). *Electron Holography*. Berlin: Springer.

Typke, D. & Dierksen, K. (1995). Determination of image aberrations in high-resolution electron microscopy using diffractograms and cross-correlation methods. *Optik* **99**, 155–166.

Uhlemann, S. & Haider, M. (1998). Residual wave aberrations in the first spherical aberration corrected transmission electron microscope. *Ultramicroscopy* **72**, 109–119.

Urban, K., Kabius, B., Haider, M. & Rose, H. (1999). A way to higher resolution: Spherical-aberration correction in a 200 kV transmission electron microscope. *J Elect Microsc* **48**, 821–826.

Van Dyck, D., Op de Beeck, M. & Coene, W. (1993). A new approach to object wavefunction reconstruction in electron microscopy. *Optik* **93**, 103–107.

Wang, Y.C., Fitzgerald, A., Nelson, E.C., Song, C., O'Keefe, M.A. & Kisielowski, C. (1999). Effect of correction of the 3-fold astigmatism on HREM lattice imaging with information below 100 pm. In *Proceedings of the 57th Annual Microscopy Society of America Meeting*, pp. 822–823. New York: Springer-Verlag.

Zemlin, F., Weiss, K., Schiske, P., Kunath, W. & Herrmann, K.-H. (1978). Coma-free alignment of high-resolution electron microscopes with the aid of optical diffractograms. *Ultramicroscopy* **3**, 49–60.

Zernike, F. (1942*a*). Phase contrast, a new method for the microscopic observation of transparent objects, Part I. *Physica* **9**, 686–698.

Zernike, F. (1942*b*). Phase contrast, a new method for the microscopic observation of transparent objects, Part II. *Physica* **9**, 974–986.

Zernike, F. (1955). How I discovered phase contrast. *Science* **121**, 345–349.